

Highlighting research from Group L03, Institute of Physics,
Chinese Academy of Sciences.

Effects of line defects on the electronic and optical properties
of strain-engineered WO_3 thin films

We report the discovery of a new line defect, and the
modification of electronic structures induced by this line defect
in strain-engineered WO_3 epitaxial films.

As featured in:



See Chen Ge, Kui-juan Jin et al.,
J. Mater. Chem. C, 2017, 5, 11694.

Cite this: *J. Mater. Chem. C*, 2017,
5, 11694

Effects of line defects on the electronic and optical properties of strain-engineered WO₃ thin films†

Jing-ting Yang,[‡] Chao Ma,[‡] Chen Ge,[‡] Qing-hua Zhang,^a Jian-yu Du,^a
Jian-kun Li,^a He-yi Huang,^{ab} Meng He,^a Can Wang,^a Sheng Meng,^{ac} Lin Gu,^{abc}
Hui-bin Lu,^a Guo-zhen Yang^{abc} and Kui-juan Jin^{*abc}

Tungsten oxide (WO₃) is a promising material with a wide spectrum of important applications including smart windows, clean energy, and gas sensing. A variety of ionic defects in WO₃ have attracted much attention due to their ability to greatly enhance these functionalities. In this work, we report the discovery of a new line defect in WO₃ epitaxial thin films obtained via a strain engineering approach, and the modification of electronic structures in strain engineered WO₃ films. This unique line defect observed by scanning transmission electron microscopy (STEM) can be regarded as an A-site deficient pseudo-perovskite cell, rotated by 45 degrees. By analyzing the distinct electronic and optical properties of these strain-engineered line defect phases, we show the emergence of an intriguing local hole channel along the line defects and highly tunable band structures, which can be harnessed in photocatalysis and electrochromism. Such defect effects induced by strain can lead to novel functionalities in artificially designed oxide heterostructures.

Received 26th August 2017,
Accepted 23rd October 2017

DOI: 10.1039/c7tc03896h

rsc.li/materials-c

1. Introduction

Owing to their outstanding electrochromic, catalytic and gas-sensing properties, tungsten oxides have attracted intense research interest, and emerged as one of the key materials in many multifunctional devices.^{1–10} Tungsten oxides have a complex defect chemistry including accommodation of large concentrations of oxygen defects.^{11,12} Substoichiometric phases with defect configurations can endow tungsten oxides with abundant functional merits.^{3,11} Crystalline defects significantly affect the bandgap, free-electron density, and Fermi level of tungsten oxides, resulting in a large modulation of conductivity.^{13–15} The defects can form open structures, consisting of trigonal, quadrangular, pentagonal or hexagonal tunnels,^{3,12} which make tungsten oxides a good host for cation accommodation and diffusion with wide applications in electrochromism and Li batteries.^{16–19} Moreover, defects on the surface of WO_x used as a catalyst would greatly facilitate bonding interactions with gas or liquid, and highly improve the catalytic activity in certain reactions.^{1,20} Besides the applications in chromism and catalysis, strong near-infrared absorption in

substoichiometric WO_x ($x < 2.9$) makes it a new candidate for photothermal/photodynamic applications.^{21,22} Therefore, constructing new defects and understanding their nature may be of great importance in future application studies.

Strain between oxide films and substrates can be harnessed to generate defects.^{23–27} Different contents of oxygen deficiency were found in La_{0.5}Sr_{0.5}CoO_{3–δ} (LSCO) thin films grown on two substrates, NdGaO₃ (NGO) and La_{0.3}Sr_{0.7}Al_{0.65}Ta_{0.35}O₃ (LSAT), and these two films exhibit different magnetic properties.²⁶ The structure of WO₃ can be viewed as an A-site deficient perovskite (ABO₃). Due to the absence of the A-site cation, corner-sharing WO₆ octahedral units are easily tilted and distorted to form six crystallographic phases.¹¹ As a result, strain engineering is a very suitable approach to tune the structural distortions in WO₃ films. In the past two years, strain-induced changes in the structure and properties of WO₃ epitaxial films have drawn increasing attention.^{28–34} Yun *et al.* observed a well-aligned ferroelastic twin structure in monoclinic WO₃/YAlO₃ (YAO) epitaxial thin films.²⁸ The metastable tetragonal phase of WO₃ can be stabilized by growing it on LaAlO₃ (LAO) or SrTiO₃ (STO).^{29,30} Du *et al.* performed a pioneering work where they observed three types of planar defects by STEM, and revealed how WO₃ epitaxial films accommodate the in-plane lattice misfit on the atomic scale.³⁰ Wang *et al.* used WO₃/SNT0 (Nb:SrTiO₃) thin films to investigate the ion-intercalation-induced phase transformation of WO₃.³¹ Based on the above investigations, we can deduce that strain can significantly affect the structure and properties of WO₃, and offers an opportunity to explore novel structures and intriguing functionalities.

^a Beijing National Laboratory for Condensed Matter Physics, Institute of Physics, Chinese Academy of Sciences, Beijing 100190, China. E-mail: gechen@iphy.ac.cn, kjjin@iphy.ac.cn

^b School of Physical Sciences, University of Chinese Academy of Science, Beijing 100049, China

^c Collaborative Innovation Center of Quantum Matter, Beijing 100871, China

† Electronic supplementary information (ESI) available. See DOI: 10.1039/c7tc03896h

‡ These authors contributed equally to this work.

In the present work, we fabricated WO_3 films with a tetragonal phase on different perovskite oxide substrates, LAO, LSAT and STO, by using the pulsed laser deposition (PLD) technique. We found a new type of line defect by employing advanced high-resolution analytical STEM. The line defect appearing in STEM images corresponds to a pseudo-perovskite cell rotated by 45 degrees. In agreement with the STEM results, density functional theory plus U (DFT+ U) calculations confirmed that line defects form more easily in WO_3 thin films having a larger lattice mismatch. Moreover, from DFT+ U investigations, we found that the electronic and optical properties of WO_3 films are significantly modified by manipulating the strain degree of freedom. The unique ability of line defects in WO_3 providing for a directional tunnel for ion intercalation may be helpful in designing electrochromic and catalytic devices, such as electrochromic photonic crystals, and ion batteries.^{16–19,35}

2. Results and discussion

2.1 Structure analysis of WO_3 thin films

WO_3 thin films with different thicknesses were deposited by PLD. Details of the growth conditions are given in the Experimental section. Here, LAO, LSAT, and STO were employed as substrates to engineer the stress on tetragonal WO_3 films. LAO, LSAT, and STO are cubic perovskites with lattice constants of 3.788 Å, 3.868 Å, and 3.905 Å, respectively.^{36,37} The lattice of WO_3 can be viewed as a pseudo-perovskite with the lattice constants $a_{\text{pc}} = 3.712$ Å, $c_{\text{pc}} = 3.91$ Å, respectively, where the subscript “pc” denotes “pseudo-cubic”.¹¹ Therefore, the lattice mismatches between WO_3 and substrates, defined as $\varepsilon = (a_s - a_f)/a_s$, are 2.0%, 4.0%, and 4.9% for films deposited on LAO, LSAT and STO, respectively. The out-of-plane X-ray diffraction (XRD) patterns (20° to 80°) show only peaks from the (00l) diffractions of WO_3 films and perovskite substrates (Fig. S1, ESI[†]), indicating that all these thin films are fabricated along the c -axis with a good single phase. The calculated out-of-plane lattice constants are 3.660 Å, 3.665 Å and 3.669 Å for films grown on LAO, LSAT, and STO, respectively. Satellite peaks positioned around WO_3 (001) diffraction peaks can be observed in WO_3 thin films with thicknesses of 10 to 50 nm (Fig. S2, ESI[†]), confirming the high quality of all these films. In order to further carry out the structural analysis of these films, we measured the $(\bar{1}03)$ peak by using the reciprocal space mapping (RSM) technique. RSM around $(\bar{1}03)$ peak in Fig. 1a confirms a coherent growth of WO_3 films on the LAO substrate, while the reciprocal space point of simplified cubic bulk (~ 3.7 Å) is marked by a red hollow symbol.³⁰ WO_3 films grown on LSAT and STO substrates with a larger lattice mismatch appear to be partially relaxed in Fig. 1b and c. From the peak positions, we calculated the in-plane lattice constants to be 3.752 Å, 3.739 Å, and 3.720 Å for films grown on LAO, LSAT, and STO, respectively. Owing to the lattice relaxation of the films on large lattice-mismatch substrates, the in-plane and out-of-plane lattice constants of the WO_3 films decrease and increase with a larger lattice mismatch, respectively (Fig. S2, ESI[†]). Moreover, ϕ scans of the (101) reflection in Fig. 1d indicate a fourfold symmetry for all these thin films, which

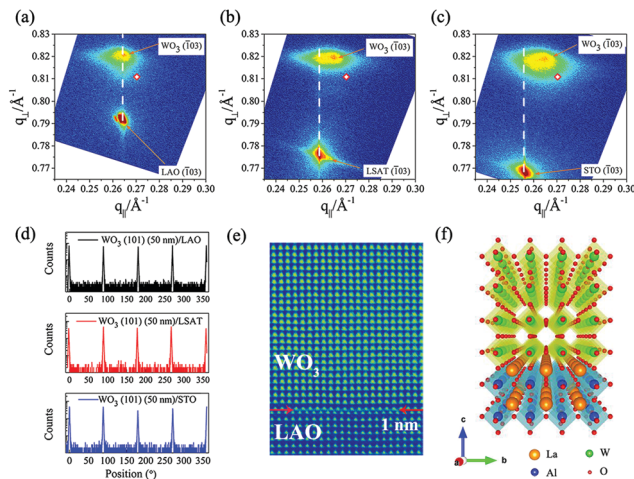


Fig. 1 Structure analysis of WO_3 thin films. (a–c) RSMs around the $(\bar{1}03)$ Bragg reflection of 50 nm thick WO_3 films grown on (001)-oriented (a) LAO, (b) LSAT, and (c) STO substrates. (d) ϕ scans around (101) reflection of 50 nm thick WO_3 thin films deposited on LAO, LSAT, and STO. (e and f) HAADF micrograph of a WO_3 thin film grown on LAO (e), and the corresponding schematic (f).

corresponds to a tetragonal structure. Peak intensities of ϕ scans are on the same order of magnitude, further indicating high film uniformity. All these X-ray diffraction results verify that the WO_3 thin films were epitaxially deposited on the perovskite substrates and the phase of our WO_3 films can be described in terms of a tetragonal unit cell, in agreement with recent works.^{29,30}

We employed atomic force microscopy (AFM) to characterize the surface smoothness of the grown films. The root-mean-square roughness is on the order of magnitude of 100 pm and increases with increasing lattice misfit (Fig. S3, ESI[†]). These data show that our grown WO_3 films have atomically flat surfaces. X-ray photoelectron spectroscopy (XPS) spectra indicate that only W^{6+} is present at the surface of the 50 nm thick WO_3 epitaxial films (Fig. S4, ESI[†]). Furthermore, we utilized aberration-corrected STEM to characterize the quality of the WO_3 thin films on the atomic scale. Fig. 1e shows a high-angle annular dark-field (HAADF) micrograph of a WO_3 thin film grown on LAO. The contrast in HAADF micrographs is known to exhibit a $Z^{1.7}$ dependence, where Z is the atomic number.³⁸ Then the spots with the largest contrast represent the W atoms. From the STEM image, the film appears to be coherently grown on the LAO substrate and there is an atomically sharp interface indicated by the red arrows. A schematic of a c -axis-oriented WO_3 film epitaxially deposited on the LAO substrate is exhibited in Fig. 1f.

2.2 Line defects induced by strain

Interestingly, a small number of line defects were probed at the interface between WO_3 and LAO by STEM. Fig. 2a shows a STEM image, taken along the $[100]$ direction of a WO_3 film grown on LAO. The red arrows indicate the location of the epitaxial interface. Line defects marked by black and orange boxes in Fig. 2a are enlarged in Fig. 2b and c, respectively. Most of the line defects extend only through a part of the specimen. The HAADF image viewed along the $[100]$ direction combines

the signal of the W atoms in the defect-free lattice (marked by a purple circle) and those in the line defects (marked by red and magenta circles), mainly showing an octagonal tungsten atomic arrangement in Fig. 2b. Fig. 2c displays a line defect running through the entire film along the [100] direction. This line defect appears as a pseudo-cubic perovskite cell rotated by 45 degrees (marked by a red circle) around the defect core, while one or more tungsten atoms (marked by a magenta circle) intercalate in the pentagonal interstices due to the rotation. Fig. 2d shows the atomic structural model of the line defect based on DFT+*U* calculations. Concerning the tetragonal phase of the thin film, the line defect propagates only along the *a*- and *b*-axis, as its propagation is forbidden along the *c*-axis. As the strain increases, the number of line defects increases remarkably by using the LSAT and STO substrates, as shown in Fig. 2e and f.

Moreover, we examined the spatial distribution of the line defects in these films. The line defects distribute only within ~ 6 nm away from the WO₃/LAO interface, ~ 7.6 nm away from

the WO₃/LSAT interface, and ~ 9 nm away from the WO₃/STO interface (Fig. S5, ESI†). Above these regions, the thin film recovers a defect-free structure. Considering the variation in the number of line defects and the defect distribution mentioned above, the generation of line defects appears as one way to release the strain induced by the lattice mismatch. A small expansion of the area with line defects can be clearly observed, as shown in Fig. 2c. The rotation of the pseudo-perovskite cell shortens the W–W bond (marked by the blue line in Fig. 2d), and enhances mutual repulsion between the W atoms, and then leads to the expansion of line defects. The expansive line defect compresses the adjacent WO₃ and decreases the in-plane lattice constants of the adjacent lattices to release the strain of the film. Compared to a misfit dislocation, the line defect releases the tensile strain more gradually in the film. Actually, line defects, commonly dominated by edge dislocations, screw dislocations, and disclinations, were rarely observed in experiments.^{39–41} The first discovery of line defects in perovskite oxides besides dislocations was reported in NdTiO₃/STO thin films by Jeong *et al.* in 2016.⁴² This line defect contains a perovskite cell rotated by 45 degrees with directionality, which is very similar to our defects in WO₃ thin films.

In addition, we found few planar defects in WO₃/LSAT and WO₃/STO (Fig. S6, ESI†). These planar defects were the cases for investigations made by Du *et al.* on WO₃/STO films.³⁰ Planar defects appear at the interface, just like an intercalated column of tungsten atoms along the [001] direction. The defect compresses the adjacent lattice and allows reducing the lattice parameter to accommodate the strain at the interface. In our case, planar defects were not observed in the WO₃/LAO films. Thus, the planar defect is another way to release the strain, but its appearance needs a larger lattice mismatch, compared to the formation of the line defect.

2.3 The effect of line defects on material properties

To better understand the underlying mechanism and physical properties behind line defects, we performed DFT+*U* calculations. Details of calculations are given in the Experimental section. We only considered the line defects with a rotated configuration in which the WO₃ stoichiometry is unchanged for simplifying the calculation. We constructed the $a \times 4a \times 4c$ supercell with corner-shared oxygen octahedra to accommodate the line-defect. The modeled atomic structure can be seen in Fig. 3a, where the four [WO₆]-octahedra as a whole at the center rotate 45° around the center simultaneously. Owing to the line defect, the oxygen ions in the WO₂-plane (*ac*-plane in Fig. 3a) form four pentagons at the four corners, four trigons in the middle of the four edges, and one tetragon at the center, respectively. These vacant spaces allow for cation accommodation and diffusion, which are similar to the structural apertures in many substoichiometric tungsten oxides.^{3,12,43} Considering the wide range of electrochromic applications of substoichiometric tungsten oxides, line defects have high potential for improved performance in functional applications such as ion batteries and electrochromism.^{16,17} The lattice constant *a* was set to be a series of values to simulate the bi-axial strain imposed on the film by different substrates.

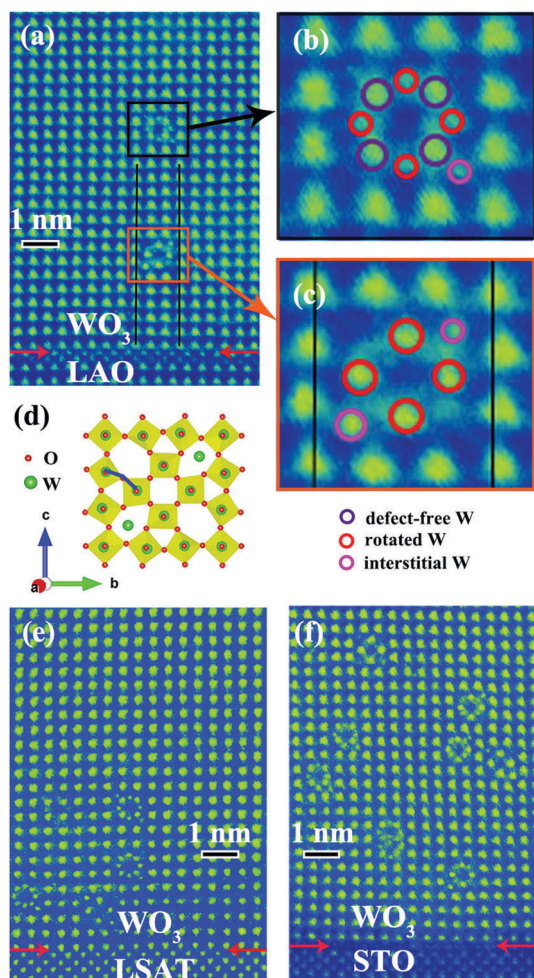


Fig. 2 STEM images of WO₃ films with line defects. (a, e and f) STEM images of WO₃ films grown on LAO (a), LSAT (e), and STO (f) substrates at the interface viewed along the [100] direction. In (a), two black lines were drawn as a reference to show the expansion of the area with line defects. (b and c) The enlarged parts of line defects (b and c) marked by black and orange boxes in panels (a). (d) A structural model for line defects based on DFT calculation.

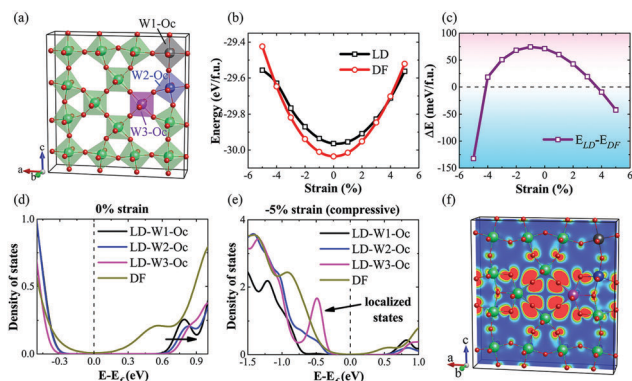


Fig. 3 Relative energies and electronic structures calculated by DFT+U. (a) The atomic structure of the defective supercell. In the labels, “W1”, “W2”, and “W3” represent different W sites; “Oc” is short for “Octahedron”, so that “W1-Oc” represents the WO_6 octahedron at the W1 site. (b) Total energy per WO_3 formula unit cell (f.u.) of a defect-free (E_{DF}) and a defective supercell (E_{LD}) versus the lattice mismatch. (c) Difference of energy per formula unit cell (ΔE) between a defect-free unit cell and a defective supercell. The negative value of ΔE means the defective supercell is energetically preferable. (d and e) Represent the density of states for various WO_6 octahedra with 0% and -5% strain, respectively. (f) The 2D contour map of charge density taken through the (0, 2, 0) plane, corresponding to the localized states as shown in (e). Contour levels (in B-G-R scale) are between 0 (blue) and $0.012 \text{ e } \text{\AA}^{-3}$ (red). The localization is around the line defect.

With each bi-axial strain applied, the lattice constant c and ion positions were fully relaxed. The strain is defined in the introduction part, where the positive values refer to expansion, while the negative values correspond to compression. Fig. 3b and c present the calculated total energy per WO_3 formula unit cell (f.u.) of a supercell containing a line defect (E_{LD}) and a defect-free unit cell (E_{DF}) versus strain. ΔE is defined as E_{LD} minus E_{DF} . Regardless of whether under tensile or compressive stress, the value of ΔE can be negative with a large enough lattice misfit. In other words, the calculated results imply that the WO_3 thin film tends to form line defects to reduce the system energy in the presence of a large lattice mismatch. On the other hand, DFT+U calculations also reveal the expansion of line defects. Under a lattice mismatch of 5%, the length of the W–W bond (marked by the blue line in Fig. 2d) in line defects is shorter than that within the defect-free region according to the calculation. The calculated c/a ratios of the line defects and defect-free unit cells under 5% strain are 0.9417, and 0.9441, respectively, indicating a relatively large in-plane constant in line defects. This is in agreement with the expansion observed by STEM results in Fig. 2c. Based on the above results, we can conclude that the generation of line defects could be a way to release strain in epitaxial WO_3 films induced by the substrates.

In order to gain more insight into this line defect, we investigated its electronic properties by extracting the density of states (DOS). There are five inequivalent W atoms, which form a pentagon at one of the four corners, according to the symmetry of the model structure. Here, three of them differ most obviously from each other. We isolated the three WO_6 -octahedra which are labeled “W*i*-Oc” ($i = 1, 2, \text{ and } 3$) as shown in Fig. 3a, where W3 locates in the line defect area. The corresponding DOS is calculated by summing up the DOS of the

tungsten atoms W*i* and half of the DOS of the six oxygen atoms in one octahedron. Above all, introducing the line defect makes the DOS more smooth (Fig. S7, ESI[†]). Compared to the defective unit cells, the DOS of the defective-free unit cell has more remarkable peaks. Moreover, the band gap and electronic hybridizations will be altered as line defects are introduced. As shown in Fig. 3d, the conduction band minimum (CBM) is pushed higher in the defective structure compared with that in the defect-free unit cell, indicating that the band gap is enlarged by the line defect. The higher CBM of WO_3 can shorten the energy difference between the H^+/H_2 redox level and CBM, which is beneficial for hydrogen generation in photoelectrocatalysis.⁴⁴ More interestingly, a peak in the DOS of the W3-octahedron (at the line defect) will appear below the valence band maximum (VBM) in the 5% compressive strain situation as shown in Fig. 3e. Fig. 3f is a 2D-contour map of charge density corresponding to the DOS peak in Fig. 3e. These states spatially localized around the line defect mainly distribute in O 2p orbitals. The small number of states in the W 5d orbitals comes from the hybridization between the W 5d and O 2p orbitals. It may be related to the change in the coordination environment under 5% compressive strain. The coordination number of W3 becomes 7, and thus the corresponding WO_6 -octahedron deforms to a WO_7 -decahedron (Fig. S8a, ESI[†]). In comparison, the coordination environment of the W atoms is not changed without strain or with 5% tensile strain (Fig. S8b and c, ESI[†]). Furthermore, as shown from the charge density distributions of the highest occupied band (the lower panels in Fig. S8, ESI[†]), this localized electronic structure is only observed in the compressed supercell, indicating that it comes from the combination of the line defect and the compressive strain. From these results, it is expected that doping holes would form a local conduction channel along the line defect with the compressive strain.

In order to evaluate the consequent change in the optical properties, we calculated the optical absorption coefficients. The optical absorption of the cubic unit cell without strain is isotropic. As shown in Fig. 4a, the optical absorption appears to be anisotropic upon introducing the line defect: the absorption edge along the line defect shifts towards lower energy within the visible range (380–780 nm) with respect to that of the defect-free structure, indicating the enhancement of absorbing low energy photons along the line defect. Moreover, the absorption of the high energy photons ($> 3.1 \text{ eV}$) is also enhanced along the other two directions. As shown in Fig. 4b, the strain would remarkably modify the optical gap of the defective structure. Applying a compressive strain enlarges the optical gap, while a tensile strain decreases the optical gap. In addition to the narrowing of the optical gap under tensile strain, the electronic band gap of the defective supercell also decreases considerably, for example, 35% (from 1.12 eV to 0.73 eV by DFT+U band structure calculations) by applying 5% strain. All the transport data of the WO_3 films deposited on the three substrates show a typical semiconductor behavior (Fig. S9, ESI[†]). The resistivity of the WO_3 films decreases with a larger tensile strain (Fig. S9, ESI[†]), which can be explained by the smaller band gap in

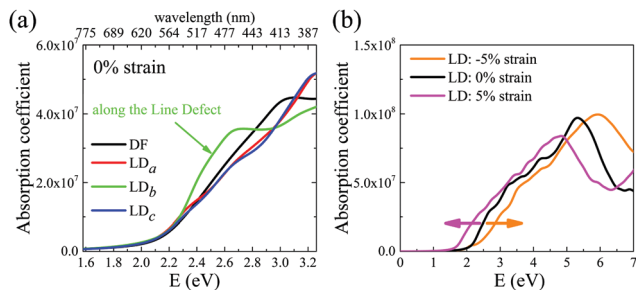


Fig. 4 Simulated optical properties. (a) Orientation-dependent absorption coefficients within the visible range (380–780 nm). The line defect runs along the *b*-direction. (b) Averaged absorption coefficients of the defective structure with various strains. Here, DF denotes the defect-free unit cell, while LD represents the unit cell with line defects.

the WO₃ films with a larger tensile strain from our DFT calculations. The band gap modulation results from the complex hybridizations between the W and O atoms, due to the change in W–O bond lengths by strain. The band gap and optical gap narrowing *via* tensile strain for defect-free unit cells are almost the same as those in the defective supercells, indicating that tensile strain can be used to effectively decrease the band gap of WO₃ films. The dramatically narrowed band gap can significantly enhance the utilization of solar energy in photoelectrochemical generation.⁴⁵ For example, Y. C. Nah *et al.* observed a significantly enhanced photocurrent in the visible light region for a nitrogen doped WO₃ layer, which has a smaller band gap (~ 1.9 eV) than intrinsic WO₃.⁴⁶

3. Conclusions

In summary, we have reported on the first discovery of line defects in tensile strained WO₃ thin films grown on perovskite substrates, LAO, LSAT, and STO. The crystal structure was investigated by RSM and STEM. The line defect can be viewed as an A-site deficient pseudo-perovskite cell rotated by 45 degrees with interstitial tungsten atoms. The defect preferentially propagates along the *a*- or *b*-axes near the interface and the number of defects can be tailored by strain engineering. STEM and DFT+*U* calculations revealed that the generation of line defects is a way to release the strain induced by the lattice mismatch. DFT+*U* calculations reveal that the electronic and optical properties can be remarkably modified by introducing line defects. Interestingly, as predicted from DFT+*U* calculations, doping holes would form a conduction channel along the line defect under a 5% compressive strain. Considering the unique electronic, optical, and chemical properties of line defects, strain-engineered WO₃ thin films have high potential in functional applications.

4. Experimental

4.1 Sample preparation

Tungsten oxide (WO₃) thin films were deposited on (001)-oriented LAO, LSAT, and STO substrates by the pulsed laser deposition (PLD) method. The target was prepared using WO₃ powder with 99.99% purity (Sigma-Aldrich) and sintered at 1300 °C for 12 hours.

A XeCl excimer laser with a wavelength of 308 nm was utilized with an energy density of ~ 1 J cm⁻² and a repetition rate of 2 Hz. During the deposition, the temperature was maintained at 500 °C with an oxygen pressure of 20 Pa. After deposition, the samples were *in situ* annealed for 10 minutes, and then cooled to room temperature. The film growth rate was determined to be 5.4 nm min⁻¹ using X-ray reflectivity measurements.

4.2 Characterization of samples

The surface morphology of the WO₃ films was recorded using a commercial atomic force microscopy (AFM) system (Asylum Research MFP3D). X-ray diffraction (XRD) measurements were performed using a Rigaku SmartLab instrument. The chemical states of tungsten atoms in the as-deposited WO₃ films were evaluated by X-ray photoelectron spectroscopy (XPS) (Thermo Scientific EscaLab 250Xi). The atomic structure of the WO₃ films was characterized using an ARM-200F (JEOL, Tokyo, Japan) scanning transmission electron microscope (STEM) operated at 200 kV with a CEOS Cs corrector (CEOS GmbH, Heidelberg, Germany) to cope up with the probe-forming objective spherical aberration. The transport properties were measured using a Keithley 4200 semiconductor parameter analyser connected with a probe station (Lake Shore).

4.3 DFT calculations

DFT calculations were performed within the generalized gradient approximation (GGA) as implemented in the Vienna Ab initio Simulation Package (VASP).⁴⁷ The PBE exchange and correlation functional was adopted.⁴⁸ The projector augmented wave method (PAW)⁴⁹ was used to treat the core and valence electrons with the following electronic configurations: 5p⁶5d⁴6s² (W) and 2s²2p⁴ (O). We included an effective Hubbard term $U_{\text{eff}} = U - J$ using Dudarev's approach to treat the 5d orbitals of W ($U_{\text{eff}} = 6.2$ eV).⁵⁰ The energy cutoff of the plane wave basis set was taken as 520 eV for all calculations. For optimizations of all these three structures, atomic positions were relaxed until the energy differences were within 1×10^{-6} eV and all forces were smaller than 1 meV Å⁻¹. For simplicity, tilts and rotations of oxygen octahedra were not considered in the reference defect-free structure. The unstrained unit cell in our calculations is cubic (*Pm* $\bar{3}$ *m* symmetry). Thus the unit cell deforms into the *P4/mmm* tetragonal structure under in-plane strain. We constructed the $1 \times 4 \times 4$ supercell with corner-shared oxygen octahedra to accommodate the line-defect. The corresponding lattice constants are *a*, 4*a*, and 4*c* respectively. The lattice constant *a* is the same as that in the *P4/mmm* structure and *c* is fully relaxed under a certain strain.

Conflicts of interest

There are no conflicts of interest to declare.

Acknowledgements

This work was supported by the National Key R&D Program of China (No. 2017YFA0303604), the National Basic Research

Program of China (No. 2014CB921001), the National Natural Science Foundation of China (No. 11674385, 11404380, 51522212, and 51421002), the Key Research Program of Frontier Sciences CAS (No. QYZDJSSW-SLH020), and the Strategic Priority Research Program (B) of the Chinese Academy of Sciences (No. XDB07030200).

References

- 1 Y. H. Li, P. F. Liu, L. F. Pan, H. F. Wang, Z. Z. Yang, L. R. Zheng, P. Hu, H. J. Zhao, L. Gu and H. G. Yang, *Nat. Commun.*, 2015, **6**, 8064.
- 2 R. Abe, H. Takami, N. Murakami and B. Ohtani, *J. Am. Chem. Soc.*, 2008, **130**, 7780.
- 3 S. Cong, F. Geng and Z. Zhao, *Adv. Mater.*, 2016, **28**, 10518.
- 4 N. C. D. Nath, S. Y. Choi, H. W. Jeong, J.-J. Lee and H. Park, *Nano Energy*, 2016, **25**, 51.
- 5 P. Grey, L. Pereira, S. Pereira, P. Barquinha, I. Cunha, R. Martins and E. Fortunato, *Adv. Electron. Mater.*, 2016, **2**, 1500414.
- 6 P. Barquinha, S. Pereira, L. Pereira, P. Wojcik, P. Grey, R. Martins and E. Fortunato, *Adv. Electron. Mater.*, 2015, **1**, 1500030.
- 7 S. K. Deb, *Sol. Energy Mater. Sol. Cells*, 2008, **92**, 245.
- 8 J. Y. Zheng, Z. Haider, T. K. Van, A. U. Pawar, M. J. Kang, C. W. Kim and Y. S. Kang, *CrystEngComm*, 2015, **17**, 6070.
- 9 L. Liang, K. Li, C. Xiao, S. Fan, J. Liu, W. Zhang, W. Xu, W. Tong, J. Liao, Y. Zhou, B. Ye and Y. Xie, *J. Am. Chem. Soc.*, 2015, **137**, 3102.
- 10 Y. Liu, L. Liang, C. Xiao, X. Hua, Z. Li, B. Pan and Y. Xie, *Adv. Energy Mater.*, 2016, **6**, 1600437.
- 11 H. Zheng, J. Z. Ou, M. S. Strano, R. B. Kaner, A. Mitchell and K. Kalantar-zadeh, *Adv. Funct. Mater.*, 2011, **21**, 2175.
- 12 A. Polaczek, M. Pekata and Z. Obuszko, *J. Phys.: Condens. Matter*, 1994, **6**, 7909.
- 13 W. Sahle and M. Nygren, *J. Solid State Chem.*, 1983, **48**, 154.
- 14 J. M. Berak and M. J. Sienko, *J. Solid State Chem.*, 1970, **2**, 109.
- 15 Z. Zhang, H. X. Wei, G. F. Ma, Y. Q. Li, S. T. Lee and J. X. Tang, *Appl. Phys. Lett.*, 2013, **103**, 133302.
- 16 K. Huang and Q. Zhang, *Nano Energy*, 2012, **1**, 172.
- 17 A. Martinez-dela Cruz, U. Amador, J. Rodriguez-Carvajal and F. Garcia-Alvarado, *J. Solid State Chem.*, 2005, **178**, 2998.
- 18 T. Sumida, Y. Wada, T. Kitamura and S. Yanagida, *Chem. Lett.*, 2002, 180.
- 19 S.-L. Kuai, G. Bader and P. V. Ashrit, *Appl. Phys. Lett.*, 2005, **86**, 221110.
- 20 J. Liu, O. Margeat, W. Dachraoui, X. Liu, M. Fahlman and J. Ackermann, *Adv. Funct. Mater.*, 2014, **24**, 6029.
- 21 J. J. Qiu, Q. F. Xiao, X. P. Zheng, L. Zhang, H. Y. Xing, D. Ni, Y. Y. Liu, S. J. Zhang, Q. G. Ren, Y. Q. Hua, K. Zhao and W. B. Bu, *Nano Res.*, 2015, **8**, 3580.
- 22 Z. G. Chen, Q. Wang, H. L. Wang, L. S. Zhang, G. S. Song, L. L. Song, J. Q. Hua, H. Z. Wang, J. S. Liu, M. F. Zhu and D. Y. Zhao, *Adv. Mater.*, 2013, **25**, 2095.
- 23 S. V. Kalinin and N. A. Spaldin, *Science*, 2013, **341**, 858.
- 24 F. K. Legoues, M. Copel and R. Tromp, *Phys. Rev. Lett.*, 1989, **63**, 1826.
- 25 U. Aschauer, R. Pfenninger, S. M. Selbach, T. Grande and N. A. Spaldin, *Phys. Rev. B: Condens. Matter Mater. Phys.*, 2013, **88**, 054111.
- 26 Y. M. Kim, J. He, M. D. Biegalski, H. Ambaye, V. Lauter, H. M. Christen, S. T. Pantelides, S. J. Pennycook, S. V. Kalinin and A. Y. Borisevich, *Nat. Mater.*, 2012, **11**, 888.
- 27 E. Breckenfeld, A. B. Shah and L. W. Martin, *J. Mater. Chem. C*, 2013, **1**, 8052.
- 28 S. Yun, C.-S. Woo, G.-Y. Kim, P. Sharma, J. H. Lee, K. Chu, J. H. Song, S.-Y. Chung, J. Seidel, S.-Y. Choi and C.-H. Yang, *Appl. Phys. Lett.*, 2015, **107**, 252904.
- 29 G. Li, T. Varga, P. Yan, Z. Wang, C. Wang, S. A. Chambers and Y. Du, *Phys. Chem. Chem. Phys.*, 2015, **17**, 15119.
- 30 Y. Du, M. Gu, T. Varga, C. Wang, M. E. Bowden and S. A. Chambers, *ACS Appl. Mater. Interfaces*, 2014, **6**, 14253.
- 31 Z.-G. Wang, Y. He, M. Gu, Y.-G. Du, S. X. Mao and C. Wang, *ACS Appl. Mater. Interfaces*, 2016, **8**, 24567.
- 32 H. Kalhori, S. B. Porter, A. S. Esmaeily, M. Coey, M. Ranjbar and H. Salamati, *Appl. Surf. Sci.*, 2016, **390**, 43.
- 33 X. Leng, J. Pereiro, J. Strle, A. T. Bollinger and I. Božović, *APL Mater.*, 2015, **3**, 096102.
- 34 Y. He, M. Gu, H. Xiao, L. Luo, Y. Shao, F. Gao, Y. Du, S. X. Mao and C. Wang, *Angew. Chem., Int. Ed.*, 2016, **128**, 6352.
- 35 S.-J. Kim, S.-J. Choi, J.-S. Jang, N.-H. Kim, M. Hakim, H. L. Tuller and I.-D. Kim, *ACS Nano*, 2016, **10**, 5891.
- 36 S. E. Helali, K. Daoudi, A. Fouzri, M. Oumezzine, M. Oueslati and T. Tsuchiya, *Appl. Phys. A: Mater. Sci. Process.*, 2012, **108**, 379.
- 37 D. A. Pawlak, M. Ito, L. Dobrzycki, K. Wozniak, M. Oku, K. Shimamura and T. Fukuda, *J. Mater. Res.*, 2005, **20**, 3329.
- 38 C. Ge, K.-J. Jin, L. Gu, L.-C. Peng, Y.-S. Hu, H.-Z. Guo, H.-F. Shi, J.-K. Li, J.-O. Wang, X.-X. Guo, C. Wang, M. He, H.-B. Lu and G.-Z. Yang, *Adv. Mater. Interfaces*, 2015, **2**, 1500407.
- 39 G. I. Taylor, *Proc. R. Soc. London, Ser. A*, 1934, **145**, 362.
- 40 A. E. Romanov and V. I. Vladimirov, *Phys. Status Solidi A*, 1983, **78**, 11.
- 41 M. Murayama, J. M. Howe, H. Hidaka and S. Takaki, *Science*, 2002, **295**, 2433.
- 42 J. S. Jeong, M. Topsakal, P. Xu, B. Jalan, R. M. Wentzcovitch and K. A. Mkhoyan, *Nano Lett.*, 2016, **16**, 6816.
- 43 G. L. Frey, A. Rothschild, J. Sloan, R. Rosentsveig, R. Popovitz-Biro and R. Tenne, *J. Solid State Chem.*, 2001, **162**, 300.
- 44 C. Janáky, K. Rajeshwar, N. R. De Tacconi, W. Chanmanee and M. N. Huda, *Catal. Today*, 2013, **199**, 53.
- 45 E. L. Miller, B. Marsen, D. Paluselli and R. Rocheleau, *Electrochem. Solid-State Lett.*, 2005, **8**, A247.
- 46 Y. C. Nah, I. Paramasivam, P. Hahn, N. K. Shrestha and P. Schmuki, *Nanotechnology*, 2010, **21**, 105704.
- 47 G. Kresse and J. Furthmüller, *Phys. Rev. B: Condens. Matter Mater. Phys.*, 1996, **54**, 11169.
- 48 J. P. Perdew, K. Burke and M. Ernzerhof, *Phys. Rev. Lett.*, 1996, **77**, 3865.
- 49 G. Kresse and D. Joubert, *Phys. Rev. B: Condens. Matter Mater. Phys.*, 1999, **59**, 1758.
- 50 S. L. Dudarev, G. A. Botton, S. Y. Savrasov, C. J. Humphreys and A. P. Sutton, *Phys. Rev. B: Condens. Matter Mater. Phys.*, 1998, **57**, 1505.